

# We Know Where We Don't Know: 3D Bayesian CNNs for Uncertainty Quantification of Binary Segmentations for Material Simulations

Tyler LaBonte<sup>1,2</sup>, Carianne Martinez<sup>1</sup>, and Scott A. Roberts<sup>1</sup>

<sup>1</sup>Sandia National Laboratories\*, Albuquerque, New Mexico, USA

<sup>2</sup>University of Southern California, Los Angeles, California, USA

tlabonte@usc.edu, {cmarti5, sarober}@sandia.gov

## Abstract

Deep learning has been applied with great success to the segmentation of 3D X-Ray Computed Tomography (CT) scans. Establishing the credibility of these segmentations requires uncertainty quantification (UQ) to identify problem areas. Recent UQ architectures include Monte Carlo dropout networks (MCDNs), which approximate Bayesian inference in deep Gaussian processes, and Bayesian neural networks (BNNs), which use variational inference to learn the posterior distribution of the neural network weights. BNNs hold several advantages over MCDNs for UQ, but due to the difficulty of training BNNs, they have not, to our knowledge, been successfully applied to 3D domains. In light of several recent developments in the implementation of BNNs, we present a novel 3D Bayesian convolutional neural network (BCNN) that provides accurate binary segmentations and uncertainty maps for 3D volumes. We present experimental results on CT scans of lithium-ion battery electrode materials and laser-welded metals to demonstrate that our BCNN provides improved UQ as compared to an MCDN while achieving equal or better segmentation accuracy. In particular, the uncertainty maps generated by our BCNN capture continuity and visual gradients, making them interpretable as confidence intervals for segmentation usable in subsequent simulations.

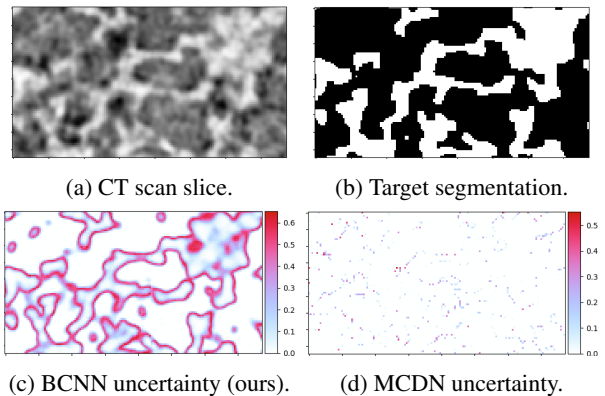


Figure 1: Zoomed Uncertainty Maps on Graphite Test Set Sample III, Slice 64. Note that the BCNN uncertainty map captures continuity and visual gradients while the MCDN uncertainty map is pixelated and uninterpretable.

## 1. Introduction

Non-destructive 3D imaging techniques allow scientists to study the interior of objects which cannot otherwise be observed. For example, radiologists use X-ray Computed Tomography (CT) to measure organ perfusion and Magnetic Resonance Imaging (MRI) to diagnose prostate carcinoma, among other applications [2, 21]. In addition to medical applications, CT scans are used in manufacturing to identify defects before a part is deployed in a production environment and to certify physical properties of materials. A critical step in the analysis of CT scans is segmentation, wherein an analyst labels each voxel in a scan (e.g., as a tumor in the medical case or as a defect in the manufacturing case). However, due to the noise and artifacts found in CT scans along with human error, these segmentations are often expensive, irreproducible, and unreliable [16]. Deep learning models such as convolutional neural

\*This paper describes objective technical results and analysis. Any subjective views or opinions that might be expressed in the paper do not necessarily represent the views of the U.S. Department of Energy or the United States Government. Supported by the Laboratory Directed Research and Development program at Sandia National Laboratories, a multimission laboratory managed and operated by National Technology and Engineering Solutions of Sandia, LLC, a wholly owned subsidiary of Honeywell International, Inc., for the U.S. Department of Energy's National Nuclear Security Administration under contract DE-NA-0003525. This manuscript has been authored by National Technology & Engineering Solutions of Sandia, LLC, under Contract No. DE-NA0003525 with the U.S. Department of Energy/National Nuclear Security Administration. The United States Government retains and the publisher, by accepting the article for publication, acknowledges that the United States Government retains a non-exclusive, paid-up, irrevocable, world-wide license to publish or reproduce the published form of this manuscript, or allow others to do so, for United States Government purposes. SAND2019-12715 O

networks (CNNs) have revolutionized the automated segmentation of 3D imaging by providing a fast, accurate solution to many challenges in segmentation.

For use with high-consequence part certification, segmentation must include uncertainty quantification (UQ). When deploying critical parts, such as those in cars and airplanes, analysts must provide accurate safety confidence intervals. Recent research casts deep neural networks as probabilistic models in order to obtain uncertainty measurements. Two common UQ architectures are Monte Carlo dropout networks (MCDNs) [6] and variational inference-based Bayesian neural networks (BNNs) [1]. MCDNs are easy to implement and enable UQ in the output space with little computational cost. In contrast, BNNs measure uncertainty in the weight space, resulting in mathematically-grounded, comprehensive UQ at the cost of at least double the number of trainable parameters and increased convergence time [6]. These difficulties combined with the curse of dimensionality have prevented the successful implementation of variational inference-based BNNs in 3D domains.

Our contributions combine the previously distinct subfields of volumetric segmentation and UQ with our novel 3D Bayesian CNN (BCNN) architecture, which effectively predicts binary segmentations of CT scans of engineering materials in addition to generating interpretable, comprehensive uncertainty maps. In contrast to the theory that a variational inference-based Bayesian architecture is computationally infeasible [6, 12], especially in 3D, we show via experimental results on CT scan datasets of lithium-ion battery electrode materials and laser-welded metals that our BCNN outperforms the regularly-adapted MCDN. As shown in Figure 1, the BCNN segmentation results in a continuous uncertainty map with gradients that enable uncertainty quantification in numerical simulations that are sensitive to variances in geometry. To the best of our knowledge, our BCNN is the first variational inference-based model designed for segmentation and UQ in a 3D domain.

## 2. Related Work

In this section, we describe recent publications in volumetric segmentation and UQ which enabled the success of our BCNN.

### 2.1. Volumetric Segmentation

The problem of volumetric segmentation has seen much high-impact work in the past three years. The 2D Fully Convolutional Network [14] and U-Net [26] led Milletari *et al.* [17] to propose the first 3D CNN for binary segmentation of MRI images, called V-Net. At around the same time, Çiçek *et al.* [3] proposed 3D U-Net, a direct extension of the U-Net to a 3D domain. While V-Net was designed for binary segmentation of the human prostate and 3D U-Net was designed for binary segmentation of the kidney of the

*Xenopus*, they both employ an encoder-decoder architecture inspired by U-Net [17, 3]. In this technique, a 3D volume is mapped to a latent space via successive convolutional and pooling layers; this latent representation is then upsampled and convolved until it reaches the size of the original volume and outputs the resulting per-voxel segmentation [26].

While most volumetric segmentation work pertains to the medical field, 3D materials segmentation is also an active area of research due to the importance of quality segmentations in physics simulations. In 2018, Konopczyski *et al.* [11] employed fully convolutional networks to segment CT scan volumes of short glass fibers, outperforming traditional non-deep learning techniques and achieving the first accurate results in low-resolution fiber segmentation. More recently, MacNeil *et al.* [15] proposed a semi-supervised algorithm for segmentation of woven carbon fiber volumes from sparse input.

### 2.2. Uncertainty Quantification

While deep learning models often outperform traditional statistical approaches in terms of accuracy and generalizability, they do not have built-in uncertainty measurements like their statistical counterparts. Gal and Ghahramani [6] showed that predictive probabilities (i.e., the softmax outputs of a model) are often erroneously interpreted as an uncertainty metric. Instead, recent work has cast neural networks as Bayesian models via approximating probabilistic models [6] or utilized variational inference to learn the posterior distribution of the network weights [1].

#### 2.2.1 Monte Carlo Dropout Networks

Gal and Ghahramani [6] showed that a neural network with dropout applied before every weight layer (an MCDN) is mathematically equivalent to an approximation to Daniilou and Lawrence’s [4] deep Gaussian process. Specifically, one can approximate a deep Gaussian process with covariance function  $\mathbf{K}(\mathbf{x}, \mathbf{y})$  by placing a variational distribution over each component of a spectral decomposition of the covariance function; this maps each layer of the deep Gaussian process to a layer of hidden units in a neural network. By averaging stochastic forward passes through the dropout network at inference time, one obtains a Monte Carlo approximation of the intractable approximate predictive distribution of the deep Gaussian process [6]; thus the voxel-wise standard deviations of the predictions are usable as an uncertainty metric.

One of the top benefits of the MCDN is its ease of implementation; as an architecture-agnostic technique which is dependent only on the dropout layers, Monte Carlo dropout can easily be added to very large networks without an increase in parameters. As a result, MCDNs have been implemented with good results in several different applications.

In particular, Liu *et al.* [13] successfully implemented a 3D-MCDN for UQ in binary segmentations of MRI scans of the amygdala, and Martinez *et al.* [16] used V-Net with Monte Carlo dropout for UQ in binary segmentations of CT scans of woven composite materials.

While the MCDN is one of the most common UQ architectures used in deep learning, its statistical soundness has been called into question. Osband [23] argues that Monte Carlo dropout provides an approximation to the risk of a model rather than its uncertainty (in other words, that it approximates the inherent stochasticity of the model rather than the variability of the model’s posterior belief). Osband [23] also shows that the posterior distribution given by dropout does not necessarily converge as more data is gathered; instead, the posterior depends only on the interaction between the dropout rate and the model size.

### 2.2.2 Bayesian Neural Networks

Another approach to UQ in deep neural networks is Bayesian learning via variational inference (a BNN). Instead of point estimates, the network learns the posterior distribution over the weights given the dataset, denoted  $P(\mathbf{w}|\mathcal{D})$ , given the prior distribution  $P(\mathbf{w})$ . However, calculating the exact posterior distribution is intractable due to the extreme overparametrization found in neural networks. Previous work by Hinton and Van Camp [8] and Graves [7] proposed variational learning as a method to approximate the posterior distribution. Variational learning finds the parameters  $\theta$  of the distribution  $q(\mathbf{w}|\theta)$  via the minimization of the variational free energy cost function, often called the expected lower bound (ELBO). It consists of the sum of the Kullback-Leibler (KL) divergence and the negative log-likelihood (NLL), which Blundell *et al.* [1] explains as embodying a tradeoff between satisfying the complexity of the dataset (represented by the KL term) and satisfying the simplicity prior (represented by the NLL term):

$$\mathcal{F}(\mathcal{D}, \theta) = \text{KL}[q(\mathbf{w}|\theta) \parallel P(\mathbf{w})] - \mathbb{E}_{q(\mathbf{w}|\theta)}[\log P(\mathcal{D}|\mathbf{w})]. \quad (1)$$

Blundell *et al.* [1] proposed the Bayes by Backprop algorithm, which combines variational inference with traditional backpropagation to find the best approximation to the posterior in a computationally feasible manner. Bayes by Backprop works by using the gradients calculated in backpropagation to “scale and shift” the variational parameters of the posterior, thus updating the posterior with minimal additional computation [1].

One challenge associated with probabilistic weights is that all examples in a mini-batch typically have similarly sampled weights, limiting the variance reduction effect of large mini-batches [30]. Kingma and Welling [10] introduced local reparametrization, which greatly reduces the

variance of stochastically sampled weights by transforming global weight uncertainty into independent local noise across examples in the mini-batch. In a similar vein, Wen *et al.* [30] proposed the Flipout estimator, which empirically achieves ideal variance reduction by sampling weights pseudo-independently for each example. An important difference is that the local reparametrization works only for fully connected networks, while Flipout can be used effectively in fully-connected, convolutional, and recurrent networks [30].

To the best of our knowledge, there are no implementations of a 3D BCNN with variational inference such as ours in the literature. In the 2D domain, Shridhar *et al.* [27] proposed a 2D BCNN with variational inference that extended local reparametrization to convolutional networks with a double-convolution approach and Softplus normalization [27]. In contrast, we employ the Flipout estimator [30], which Shridhar *et al.* do not reference. Furthermore, Ovadia *et al.* [24] showed that 2D BCNNs with Flipout and variational inference are effective for UQ on the MNIST and CIFAR-10 datasets, but they found it was difficult to get BCNNs to work with complex datasets. We provide a solution via our 3D BCNN which is effective across multiple high-complexity datasets with tens of millions of voxels.

## 3. Methodology

In this section, we present our BCNN architecture and describe our reasoning behind several design decisions.

### 3.1. Architecture

In Figure 2, we present a schematic representation of our BCNN architecture. Similarly to V-Net, we employ an encoder-decoder architecture. The encoder half (left) of the network compresses the input into a latent space while the decoder half (right) decompresses the latent representation of the input into a segmentation map. We do not include stochastic layers in the encoder half of the network to maximize the amount of information transfer between the original volume and the latent space.

The encoder half of the network is comprised of four stages, each with two convolutional layers and normalization layers followed by a max pooling layer to reduce the size of the input. Thus, after each layer, our volume’s depth, height, and width are halved while its channels are doubled, reducing the size of our volume by a factor of four.

The decoder half of the network consists of three stages, corresponding to the first three layers of the encoder half. First, we upsample the output of the previous layer and apply convolutional and normalization layers to double our volume’s depth, height, and width while halving its channels. We then concatenate this volume with the pre-pooling output of the corresponding encoder layer; this skip connection assists in feature-forwarding through the network.

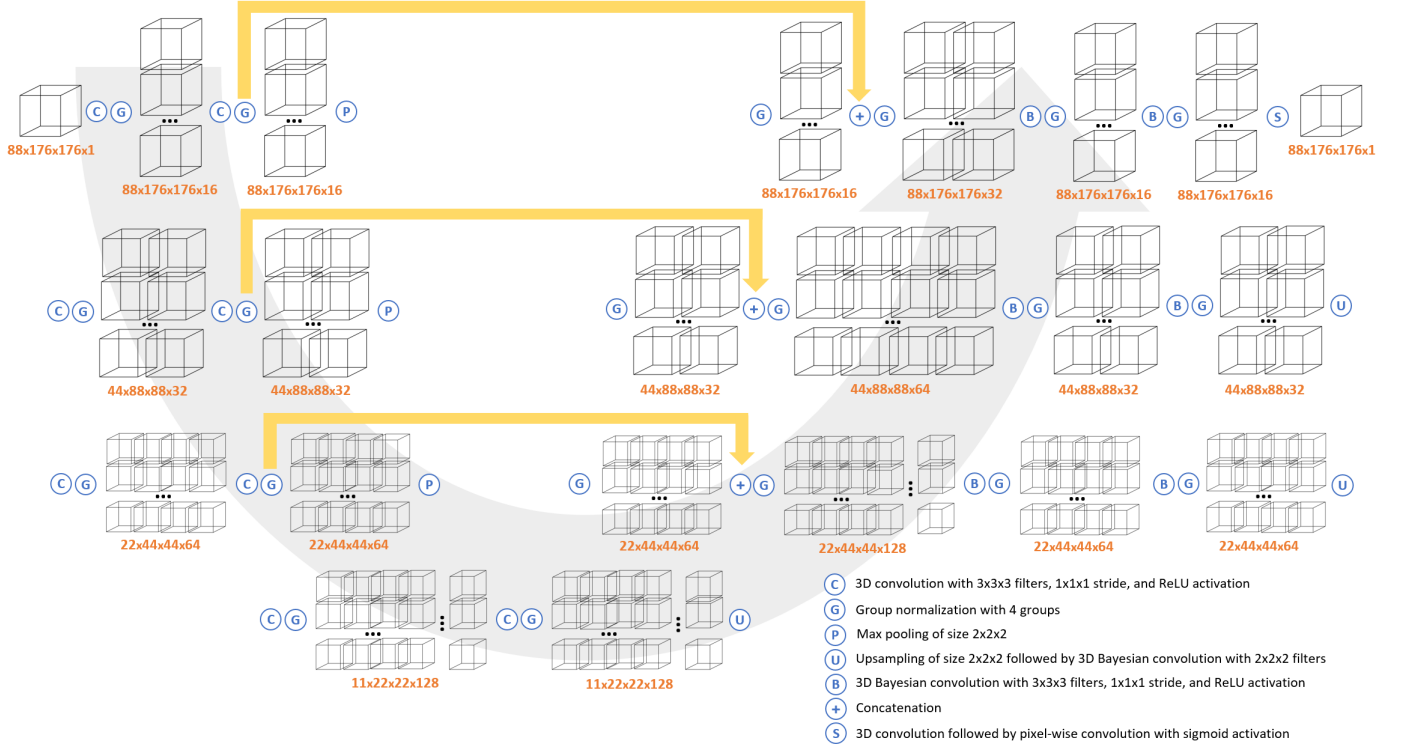


Figure 2: Schematic of our BCNN architecture with sample volume dimensions from the Graphite dataset. Best viewed in electronic format. Measurements are (depth, height, width, channels).

Then, we apply two more convolutional and normalization layers. At the end of the third stage, we apply a final convolutional layer as well as a sigmoid activation. This results in a volume of the same size as the input representing a binary segmentation probability map.

In the decoder half of the network, we implement volumetric convolutional layers with distributions over the weights. Each Bayesian convolutional layer is initialized with a prior  $P(\mathbf{w}) = \mathcal{N}(0, 1)$  and employs the aforementioned Flipout estimator to approximate the distribution during forward passes [30]. Our implementation draws from the Bayesian Layers library [29] included in TensorFlow Probability [5], which keeps track of losses representing the KL divergence of the layer’s posterior distribution with respect to its prior. Our BCNN has 1,924,964 trainable parameters, while its Monte Carlo dropout counterpart has 1,403,059.

### 3.2. Design Decisions

Since training volumes can be quite large, our batch size is constrained by the amount of available GPU memory, resulting in a batch size too small for batch normalization to accurately compute batch statistics. Thus, we implement a recent technique proposed by Wu and He [31] called group

normalization, which normalizes groups of channels and is shown to have accurate performance independent of batch size. Proper normalization was observed to be a critical factor in the convergence of our model; by tuning the number of groups used in the group normalization layers, we found that our model converged most reliably when using 4 groups.

At each downward layer  $i$ , we apply  $2^{3+i}$  filters. This was found to be more effective than a more simple model with  $2^{2+i}$  filters and a more complex model with  $2^{4+i}$  filters. We hypothesize that some minimum amount of learned parameters was necessary to produce accurate segmentations, but that with  $2^{4+i}$  filters, the overparameterization made training significantly more difficult.

We tested many priors, including scale mixture [1], spike-and-slab [18], and a normal distribution with increased variance, but found that a standard normal prior provided the best balance between weight initialization and weight exploration. Skip connections were found to slightly increase the accuracy of our predictions by forwarding fine-grained features that otherwise would have been lost in the encoder half of the network. We experimented with both max pooling and downward convolutional layers and observed negligible difference.

## 4. Experiments

In this section, we describe our datasets and detail our training and testing procedures.

### 4.1. Datasets

Two 3D imaging datasets are used to test our BCNN. The first is a series of CT scans of graphite electrodes for lithium-ion batteries, which we refer to as the Graphite dataset [20, 25]. This material consists of non-spherical particles (dark objects in the images) that are coated onto a substrate and calendared to densify. The academically manufactured (“numbered”) electrodes [20] were imaged with 325 nm resolution and a domain size of  $700 \times 700 \times (48 - 75) \mu\text{m}$ . The commercial (“named”) electrodes [25] were imaged at 162.5 nm resolution and a domain size of  $416 \times 195 \times 195 \mu\text{m}$ . Eight samples were studied, each with approximately one billion voxels. Each volume was hand-segmented using commercial tools [22]; these manual segmentations were used for training and testing. We trained our BCNN on the GCA400 volume and tested on the remaining seven electrodes.

Laser-welded metal joints comprise a second dataset, which we refer to as the Laser Weld dataset. To generate these volumes, two metal pieces are put into contact and joined with an incident laser beam. The light regions of the resulting scans represent voids or defects in the weld. The Laser Weld dataset consists of CT scans of nine laser-welded metal joint examples, each with tens of millions of voxels. Similarly to the battery materials, these volumes were manually segmented and used for training and testing. We trained a separate BCNN on samples S2, S24, and S25, testing on the remaining six held-out volumes.

For both datasets, we normalized each CT scan to have voxel values with zero mean and unit variance. Additionally, each CT scan was large enough to require that we process subvolumes of the 3D image rather than ingesting the entire scan as a whole into the neural network on the GPU.

### 4.2. Training

We use the Adam optimizer [9] with learning rate  $\alpha$  initialized at  $\alpha_0 = 0.0001$  for the Graphite dataset and  $\alpha_0 = 0.001$  for the Laser Weld dataset; this difference is necessary because the volumes in the Graphite dataset are significantly larger than those of the Laser Weld dataset. Our learning rate exponentially decays after the tenth epoch  $E$  as detailed in Equation 2; this decay was necessary for the reliable convergence of our model, likely due to its stochastic nature.

$$\alpha = \begin{cases} \alpha_0 & \text{if } E \leq 10 \\ \alpha_0 e^{10\alpha_0(10-E)} & \text{if } E > 10 \end{cases} \quad (2)$$

We use the aforementioned Bayes by Backprop algo-

rithm to train our BCNN, minimizing the variational free energy cost function as stated in Equation 1. Graves [7] notes that variational free energy is amenable to mini-batch optimization by scaling the cost for mini-batch  $i = 1, 2, \dots, M$  as:

$$\mathcal{F}_i^{\text{EQ}}(\mathcal{D}_i, \theta) = \frac{1}{M} \text{KL}[q(\mathbf{w}|\theta) \parallel P(\mathbf{w})] - \mathbb{E}_{q(\mathbf{w}|\theta)}[\log P(\mathcal{D}_i|\mathbf{w})]. \quad (3)$$

The  $1/M$  factor divides the KL divergence penalty such that it is distributed evenly over each minibatch; without this scaling, the KL divergence term dominates the equation, causing the model to converge to a posterior with sub-optimal accuracy.

We parallelized our model and trained on two NVIDIA Tesla V100 GPUs with 32GB of memory each. For our BCNN, one epoch of 1331 chunks of size  $88 \times 176 \times 176$  took approximately 17 minutes and 30 seconds with a maximum batch size of 3. We trained each model for 21 epochs on the Graphite dataset; for the Laser Weld dataset, the MCDN converged much faster, so we trained our BCNN for 27 epochs and the MCDN for 10 epochs.

### 4.3. Testing

We computed 48 Monte Carlo samples on each test volume to obtain a distribution of sigmoid values for each voxel. The Monte Carlo dropout technique is justified in representing uncertainty as the standard deviation of the sigmoid values because it approximates a Gaussian process [6]; however, the BCNN does not guarantee adherence to a normal distribution. Thus, in order to effectively compare the outputs of both networks, we represent confidence intervals on the segmentation as the second and eighth deciles of the sigmoid values, and uncertainty as the difference. We compare our results against an MCDN of identical architecture to our BCNN except with regular convolutional layers instead of Bayesian convolutional layers and spatial dropout [28] applied at the end of each stage prior to upsampling.

## 5. Results

In this section, we present inference results of our BCNN and compare its performance with the MCDN.

### 5.1. Graphite Dataset

Figure 3 shows a successful segmentation and uncertainty measurements on the GCA2000 sample from the Graphite dataset. Our BCNN provides an equivalent or better segmentation than the MCDN and produces a usable, credible uncertainty map. Figure 1 shows a zoomed-in portion of the III sample uncertainty map which highlights the continuity and visual gradients captured in our BCNN uncertainty map, while the MCDN produces uninterpretable

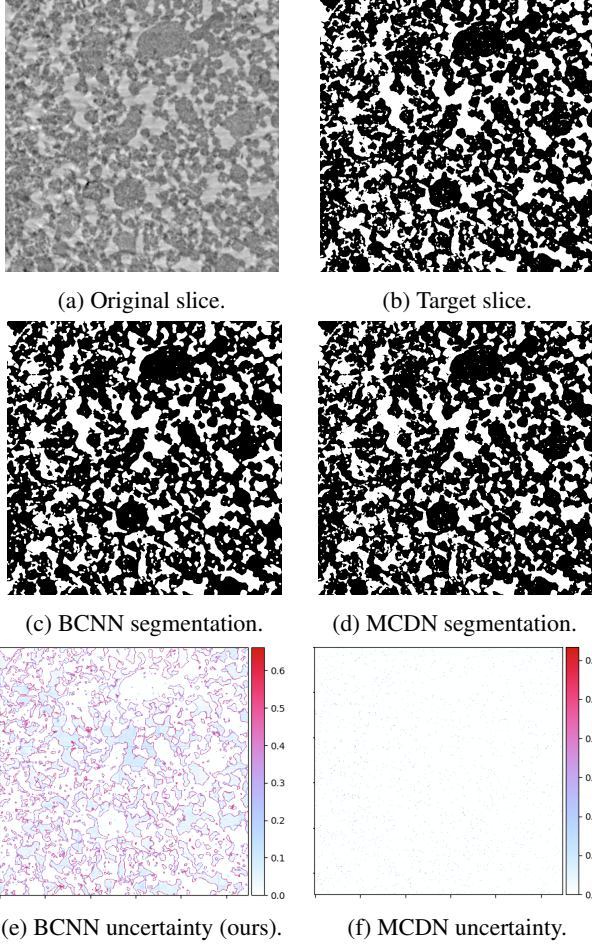


Figure 3: Results on Graphite Test Set Sample GCA2000, Slice 212. Note that our BCNN uncertainty is focused around the light gray edges of the material in the original slice, while the MCDN uncertainty is pixelated and uninterpretable.

voxel-by-voxel uncertainty measurements. We hypothesize that this is an advantage of our BCNN measuring the uncertainty in the weight space, rather than in the output space like the MCDN.

Table 1 lists a selection of descriptive statistics regarding model performance on the Graphite dataset. Our BCNN achieves a higher segmentation accuracy than the MCDN on the numbered datasets but slightly lower accuracy on the named datasets. The manual labels resulted from thresholding techniques and are known to contain inaccuracies, especially at particle boundaries. As such, we conclude that the accuracy performance of our BCNN is similar to that of the MCDN with respect to these labels, but further assessments against refined labels are left for future work.

Sample	Method	Accuracy	UQ Mean ( $\times 10^{-2}$ )
I	MCDN	0.8381	0.8162
	BCNN (ours)	0.8405	15.50
III	MCDN	0.7449	0.7703
	BCNN (ours)	0.7566	15.61
IV	MCDN	0.6979	0.9065
	BCNN (ours)	0.7116	15.76
GCA2000	MCDN	0.9734	0.2504
	BCNN (ours)	0.9695	9.391
25R6	MCDN	0.9208	0.3105
	BCNN (ours)	0.8955	9.808
E35	MCDN	0.9057	0.3399
	BCNN (ours)	0.8815	9.090
Litarion	MCDN	0.9179	0.3075
	BCNN (ours)	0.8987	8.945

Table 1: Graphite Test Set Statistics. Note that our BCNN has roughly the same accuracy performance as the MCDN. Additionally, our BCNN has an order of magnitude more uncertainty due to its increased stochasticity.

## 5.2. Laser Weld Dataset

Figure 4 shows a successful segmentation and uncertainty measurements on the S33 sample from the Laser Weld dataset. Note that the BCNN uncertainty map captures the uncertainty gradient (corresponding to the gray portion of the CT scan slice) at the top left and bottom left of the segmentation, while the MCDN uncertainty map displays a straight line. The uncertainty map contains low-uncertainty artifacts on the lines where the chunks were separated from the original CT scan volume; however, this is of little consequence because since the artifacts are significantly more low-intensity than the measured uncertainty, so they can easily be removed via a thresholding algorithm.

Table 2 lists a selection of descriptive statistics regarding model performance on the Laser Weld dataset. Note that it is slightly more difficult for our BCNN to produce accurate segmentations on the Laser Weld dataset than the Graphite dataset. While the accuracy of our BCNN prediction is usually less than a percentage point away from the MCDN and outperforms it on the S26 sample, our BCNN experiences a clear segmentation failure along the edges of the material in the S4 sample. Figure 5 shows a failure case of our BCNN on the S4 sample. Note however that the most intense areas of the uncertainty map correspond to the incorrect areas of the segmentation, indicating a successful uncertainty measurement. Thus, we use the uncertainty-based domain-shift algorithm proposed by Martinez *et al.* [16] to refine the segmentation and achieve an accuracy on par with the MCDN, also shown in Figure 5.



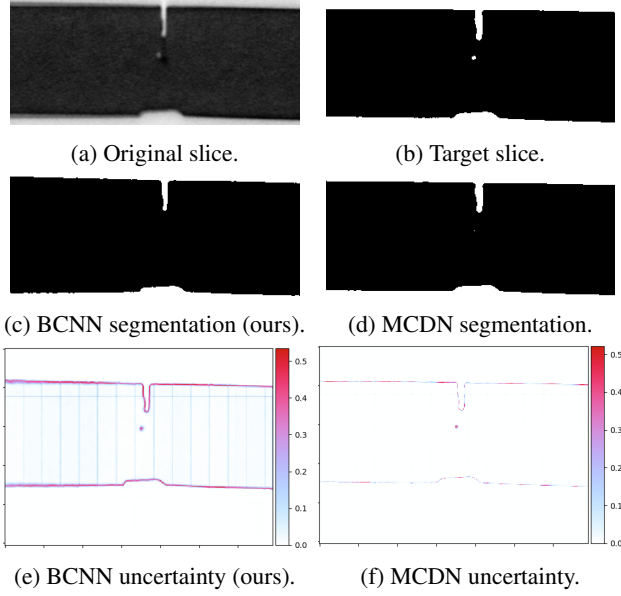


Figure 4: Results on Laser Weld Test Set Sample S33, Slice 453. Note that our BCNN uncertainty captures the visual gradients around the edges of the material, while the MCDN uncertainty displays a pixelated line at best.

Sample	Method	Accuracy	UQ Mean ( $\times 10^{-2}$ )
S1	MCDN	0.9955	0.1855
	BCNN (ours)	0.9811	2.557
S4	MCDN	0.9962	0.1935
	BCNN (ours)	0.9785	2.971
S15	MCDN	0.9963	0.2824
	BCNN (ours)	0.9932	2.509
S26	MCDN	0.9910	0.2613
	BCNN (ours)	0.9918	1.825
S31	MCDN	0.9970	0.2406
	BCNN (ours)	0.9896	1.491
S32	MCDN	0.9921	0.3121
	BCNN (ours)	0.9878	1.778
S33	MCDN	0.9960	0.2469
	BCNN (ours)	0.9861	1.735

Table 2: Laser Weld Test Set Statistics. Similarly to the Graphite dataset, our BCNN has roughly the same accuracy performance as the MCDN with an order of magnitude more uncertainty due to its increased stochasticity.

### 5.3. Validation

Validation of UQ results is a difficult subject, and there has not been much work on determining whether a model’s UQ is justified given the data. For validating our BCNN, the most relevant work in this area is due to Mukhoti and

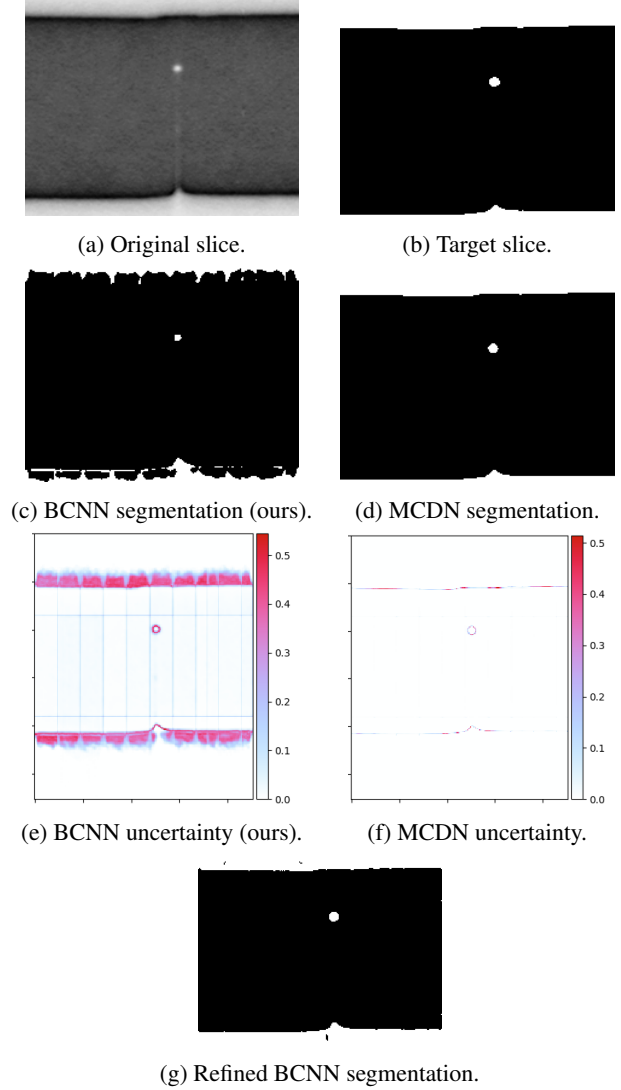


Figure 5: BCNN Segmentation Failure Case: Laser Weld Test Set Sample S4, Slice 372. Note that, while our BCNN produces a poor segmentation, its uncertainty map exactly corresponds to the areas of the image where the segmentation overpredicts. We show that the uncertainty-based refinement algorithm proposed by Martinez *et al.* [16] applied to the BCNN output with a threshold of 0.22 produces a high-accuracy segmentation.

Gal [19]. They define two desiderata for quality uncertainty maps:

1. A high probability of being accurate when the model is certain, denoted  $P(A|C)$ .
2. A high probability of being uncertain when the model is inaccurate, denoted  $P(U|I)$ .

They estimate these quantities by evaluating accuracy and uncertainty using an  $n \times n$  sliding patch; if the patch

accuracy is equal to or above a certain threshold, the entire patch is labeled accurate, and if the patch uncertainty is equal to or above a certain threshold, the entire patch is labeled uncertain. They define a metric called PAvPU (Patch Accuracy vs. Patch Uncertainty), which encodes the above two desiderata in addition to penalizing patches which are simultaneously accurate and uncertain [19].

We implement PAvPU to validate our uncertainty results using a  $3 \times 3$  patch with accuracy threshold 8/9 and uncertainty threshold equal to the mean of the uncertainty map. We detail our results in Table 3. In particular, note that our BCNN consistently outperforms the MCDN in both conditional probabilities, even doubling the  $P(U|I)$  score. Thus, we conclude that our BCNN is more effective than the MCDN in encoding the relationship between uncertainty and accuracy.

As PAvPU was designed for use with 2D semantic segmentations and not for 3D binary segmentations, it may not be sufficient to characterize the improvement in UQ achieved by the BCNN. Furthermore, the PAvPU calculation involves a penalty for patches which are accurate and uncertain, which may not necessarily be a detrimental characteristic of the segmentation [19]. This is the term that most significantly affects the PAvPU values where MCDN achieves a better result than our BCNN: our BCNN simply measures *more* uncertainty than the MCDN. Additionally, introducing this penalty term encodes the goal of training a network which is not simultaneously uncertain and accurate; however, in the Bayesian view, uncertainty and accuracy are not mutually exclusive because uncertainty quantifies the proximity of a sample to the training distribution rather than confidence in a correct segmentation. We leave the development of a more relevant uncertainty metric as future work.

#### 5.4. Advantages for Material Simulations

The objective of performing UQ on materials datasets is to obtain uncertainties which can inform and propagate throughout simulations involving said materials. For example, when simulating the performance of a sample from the Graphite dataset to bound its various physical properties, it is crucial to know the contact points of the material; the uncertainty maps generated by our BCNN represent confidence intervals on the segmentation, so we can infer the probability of a certain contact point occurring in the CT scanned material.

The voxel-by-voxel nature of the uncertainty maps given by the MCDN produce very jagged, unrealistic confidence intervals with little physical meaning. In contrast, the continuity and visual gradients of the uncertainty map generated by our BCNN enable better approximations to the actual geometric uncertainty in both the Graphite and Laser Weld materials. Our BCNN allows us to smoothly probe the un-

Sample	Method	$P(A C)$	$P(U I)$	PAvPU
Litarion, Slice 324 (Graphite)	MCDN	0.9250	0.6036	<b>0.9074</b>
	BCNN	<b>0.9963</b>	<b>0.9856</b>	0.9011
GCA2000, Slice 212 (Graphite)	MCDN	<b>0.9878</b>	0.7569	<b>0.9016</b>
	BCNN	0.9867	<b>0.8156</b>	0.7612
III, Slice 64 (Graphite)	MCDN	0.6571	0.3832	0.6841
	BCNN	<b>0.8043</b>	<b>0.7221</b>	<b>0.7642</b>
S1, Slice 176 (Laser Weld)	MCDN	0.9963	0.8198	<b>0.9050</b>
	BCNN	<b>1.0</b>	<b>1.0</b>	0.8082
S26, Slice 596 (Laser Weld)	MCDN	0.9998	0.9940	<b>0.9896</b>
	BCNN	<b>1.0</b>	<b>1.0</b>	0.8559

Table 3: PAvPU Validation Results. Note that our BCNN consistently and vastly outperforms the MCDN in the  $P(A|C)$  and  $P(U|I)$  scores, implying that our BCNN better encodes the relationship between uncertainty and accuracy. However, our BCNN underperforms in the PAvPU metric because it is penalized for being simultaneously accurate and uncertain.

certainty when performing simulations and justify each error bound we obtain with interpretable uncertainty maps, a major advantage when performing simulations for high-consequence scenarios.

## 6. Conclusion

In this work, we present a novel 3D Bayesian convolutional neural network (BCNN) for uncertainty quantification of binary segmentations, the first variational-inference based architecture to do so. By measuring uncertainty in the weight space, our BCNN provides interpretable, comprehensive UQ in 3D segmentations and outperforms the state-of-the-art Monte Carlo dropout technique. We present results in the material simulations domain, including segmentation of battery and laser weld CT scans. Our BCNN produces uncertainty maps which capture continuity and visual gradients, outperforms Monte Carlo dropout networks (MCDNs) on recent uncertainty metrics, and achieves equal or better segmentation accuracy than MCDNs in most cases. Future investigation will likely include extending our BCNN to semantic segmentation and medical applications and comparing our results with other UQ techniques such as Lakshminarayanan’s [12] deep ensembles.

## 7. Acknowledgements

We’d like to thank Kellin Rumsey for his advice on effectively comparing the uncertainty outputs of the MCDN and our BCNN. We would also like to thank Kyle Karlson for providing the Laser Weld dataset and Chance Norris for curating and segmenting the Graphite dataset.



## References

- [1] Charles Blundell, Julien Cornebise, Koray Kavukcuoglu, and Daan Wierstra. Weight uncertainty in neural networks. In *Proceedings of the 32nd International Conference on Machine Learning*, 2015.
- [2] Thorsten M. Buzug. Computed tomography. In Rüdiger Kramme, Klaus-Peter Hoffman, and Robert S. Pozos, editors, *Springer Handbook of Medical Technology*, chapter 16. 2010.
- [3] Özgün Çiçek, Ahmed Abdulkadir, Soeren S. Lienkamp, Thomas Brox, and Olaf Ronneberger. 3d u-net: Learning dense volumetric segmentation from sparse annotation. In *Proceedings of the 19th International Conference on Medical Image Computing and Computer-Assisted Intervention*, 2016.
- [4] Andreas C. Damianou and Neil D. Lawrence. Deep gaussian processes. In *Proceedings of the 16th International Conference on Artificial Intelligence and Statistics*, 2013.
- [5] Joshua V. Dillon, Ian Langmore, Dustin Tran, Eugene Brevdo, Srinivas Vasudevan, Dave Moore, Brian Patton, Alex Alemi, Matt Hoffman, and Rif A. Saurous. Tensorflow distributions. arXiv preprint 1711.10604, 2017.
- [6] Yarin Gal and Zoubin Ghahramani. Dropout as a bayesian approximation: Representing model uncertainty in deep learning. In *Proceedings of the 33rd International Conference on Machine Learning*, 2016.
- [7] Alex Graves. Practical variational inference for neural networks. In *Proceedings of the 25th Conference on Advances in Neural Information Processing Systems*, 2011.
- [8] Geoffrey E. Hinton and Drew Van Camp. Keeping neural networks simple by minimizing the description length of the weights. In *Proceedings of the 16th Conference on Learning Theory*, 1993.
- [9] Diederik P. Kingma and Jimmy Lei Ba. Adam: A method for stochastic optimization. In *Proceedings of the 3rd International Conference on Learning Representations*, 2015.
- [10] Diederik P. Kingma and Max Welling. Auto-encoding variational bayes. In *Proceedings of the 2nd International Conference on Learning Representations*, 2014.
- [11] Tomasz Konopczynski, Danish Rathore, Jitendra Rathore, Thorben Krger, Lei Zheng, Christoph S. Garbe, Simone Carmignato, and Jrgen Hesser. Fully convolutional deep network architectures for automatic short glass fiber semantic segmentation from ct scans. In *Proceedings of the 8th Conference on Industrial Computed Tomography*, 2018.
- [12] Balaji Lakshminarayanan, Alexander Pritzel, and Charles Blundell. Simple and scalable predictive uncertainty estimation using deep ensembles. In *Proceedings of the 31st Conference on Neural Information Processing Systems*, 2017.
- [13] Yilin Liu, Gengyan Zhao, Brendon M. Nacewicz, Nagesh Adluru, Gregory R. Kirk, Peter A. Ferrazzano, Martin Styner, and Andrew L. Alexander. Accurate automatic segmentation of amygdala subnuclei and modeling of uncertainty via bayesian fully convolutional neural network. arXiv preprint 1902.07289, 2019.
- [14] Jonathan Long, Evan Shelhamer, and Trevor Darrell. Fully convolutional networks for semantic segmentation. In *Proceedings of the 28th IEEE Conference on Computer Vision and Pattern Recognition*, 2015.
- [15] J. Michael L. MacNeil, Daniela M. Ushizima, Francesco Panerai, Nagi N. Mansour, Harold S. Barnard, and Dilworth Y. Parkinson. Interactive volumetric segmentation for textile micro-tomography data using wavelets and nonlocal means. *Statistical Analysis and Data Mining: The ASA Data Science Journal*, 12(4):338–353, jun 2019.
- [16] Carianne Martinez, Kevin M. Potter, Matthew D. Smith, Emily A. Donahue, Lincoln Collins, John P. Korbin, and Scott A. Roberts. Segmentation certainty through uncertainty: Uncertainty-refined binary volumetric segmentation under multifactor domain shift. In *Proceedings of the 32nd IEEE Conference on Computer Vision and Pattern Recognition: Women in Computer Vision Workshop*, 2019.
- [17] Fausto Milletari, Nassir Navab, and Seyed-Ahmad Ahmadi. V-net: Fully convolutional neural networks for volumetric medical image segmentation. In *Proceedings of the 4th International Conference on 3D Vision*, 2016.
- [18] T.J. Mitchell and J.J. Beauchamp. Bayesian variable selection in linear regression. *Journal of the American Statistical Association*, 83(404):1023–1032, 1988.
- [19] Jishnu Mukhoti and Yarin Gal. Evaluating bayesian deep learning methods for semantic segmentation. arXiv preprint 1811.12709, 2019.
- [20] Simon Miller, Patrick Pietsch, Ben-Elia Brandt, Paul Baade, Vincent De Andrade, Francesco De Carlo, and Vanessa Wood. Quantification and modeling of mechanical degradation in lithium-ion batteries based on nanoscale imaging. *Nature Communications*, 9(1):2340, June 2018.
- [21] Wolfgang Nitz. Magnetic resonance imaging. In Rüdiger Kramme, Klaus-Peter Hoffman, and Robert S. Pozos, editors, *Springer Handbook of Medical Technology*, chapter 23. 2010.
- [22] Chance Norris, Aashutosh Mistry, Partha P. Mukherjee, and Scott A. Roberts. Microstructural screening for variability in graphite electrodes. In preparation.
- [23] Ian Osband. Risk versus uncertainty in deep learning: Bayes, bootstrap and the dangers of dropout. In *Proceedings of the 30th Conference on Advances in Neural Information Processing Systems: Workshop on Bayesian Deep Learning*, 2016.
- [24] Yaniv Ovadia, Emily Fertig, Jie Ren, Zachary Nado, D. Sculley, Sebastian Nowozin, Joshua V. Dillon, Balaji Lakshminarayanan, and Jasper Snoek. Can you trust your model’s uncertainty? evaluating predictive uncertainty under dataset shift. 2019.
- [25] P. Pietsch, M. Ebner, F. Marone, M. Stampanoni, and V. Wood. Determining the uncertainty in microstructural parameters extracted from tomographic data. *Sustainable Energy Fuels*, 2:598–605, 2018.
- [26] Olaf Ronneberger, Philipp Fischer, and Thomas Brox. U-net: Convolutional networks for biomedical image segmentation. In *Proceedings of the 18th International Conference on Medical Image Computing and Computer-Assisted Intervention*, 2015.
- [27] Kumar Shridhar, Felix Laumann, and Marcus Liwicki. Uncertainty estimations by softplus normalization in bayesian

- convolutional neural networks with variational inference. arXiv preprint 1806.05978, 2019.
- [28] Jonathan Tompson, Ross Goroshin, Arjun Jain, Yann LeCun, and Christoph Bregler. Efficient object localization using convolutional neural networks. In *Proceedings of the 28th IEEE Conference on Computer Vision and Pattern Recognition*, 2015.
  - [29] Dustin Tran, Michael W. Dusenberry, Mark van der Wilk, and Danijar Hafner. Bayesian layers: A module for neural network uncertainty. 2019.
  - [30] Yeming Wen, Paul Vicol, Jimmy Ba, Dustin Train, and Roger Grosse. Flipout: Efficient pseudo-independent weight perturbations on mini-batches. In *Proceedings of the 6th International Conference on Learning Representations*, 2018.
  - [31] Yuxin Wu and Kaiming He. Group normalization. In *Proceedings of the 2018 European Conference on Computer Vision*, 2018.